








Domain nucleation across the metal-insulator transition of self-strained V_2O_3 films

Alexandre Pofelski ^{1,*} Sergio Valencia ^{2,*} Yoav Kalcheim,³ Pavel Salev ⁴ Alberto Rivera,⁵ Chubin Huang ³
Mohamad Assaad Mawass ^{2,†} Florian Kronast,² Ivan K. Schuller,⁶ Yimei Zhu ^{1,‡} and Javier del Valle ^{7,§}

¹Condensed Matter Physics and Material Science Department, Brookhaven National Laboratory, Upton, New York 11973, USA

²Department of Spin and Topology in Quantum Materials, Helmholtz-Zentrum Berlin für Materialien und Energie, 12489 Berlin, Germany

³Department of Material Science and Engineering, Technion-Israel Institute of Technology, Haifa 32000, Israel

⁴Department of Physics and Astronomy, University of Denver, Denver, Colorado 80210, USA

⁵GFMC, Departamento de Física de Materiales, Facultad de Física, Universidad Complutense, 28040 Madrid, Spain

⁶Department of Physics and Center for Advanced Nanoscience, University of California San Diego, La Jolla, California 92093, USA

⁷Department of Physics, University of Oviedo, C/ Federico García Lorca 18, 33007 Oviedo, Spain



(Received 15 December 2023; revised 21 February 2024; accepted 8 March 2024; published 27 March 2024)

Bulk V_2O_3 features concomitant metal-insulator (MIT) and structural (SPT) phase transitions at $T_C \sim 160$ K. In thin films, where the substrate clamping can impose geometrical restrictions on the SPT, the epitaxial relation between the V_2O_3 film and substrate can have a profound effect on the MIT. Here, we present a detailed characterization of domain nucleation and growth across the MIT in (001)-oriented V_2O_3 films grown on sapphire. By combining scanning electron transmission microscopy and photoelectron emission microscopy (PEEM), we imaged the MIT with planar and vertical resolution. We observed that upon cooling, insulating domains nucleate at the top of the film, where strain is lowest, and expand downwards and laterally. This growth is arrested at a critical thickness of 50 nm from the substrate interface, leaving a persistent bottom metallic layer. As a result, the MIT cannot take place in the interior of films below this critical thickness. However, PEEM measurements revealed that insulating domains can still form on a very thin superficial layer at the top interface. Our results demonstrate the intricate spatial complexity of the MIT in clamped V_2O_3 , especially the strain-induced large variations along the c axis. Engineering the thickness-dependent MIT can provide an unconventional way to build out-of-plane geometry devices by using the persistent bottom metal layer as a native electrode.

DOI: [10.1103/PhysRevMaterials.8.035003](https://doi.org/10.1103/PhysRevMaterials.8.035003)

I. INTRODUCTION

Metal-insulator transitions (MITs) have recently experienced renewed interest. The large changes in electrical, optical, and structural–mechanical properties associated with the MIT have made them attractive for applications in novel technologies such as passive cooling [1], neuromorphic computing [2–5], resistive switching [6–9], probabilistic computing [10,11], optoelectronics [12], and micromechanical oscillators [13] and actuators [14,15]. In addition, the unresolved debate about the role played by the electronic and lattice degrees of freedom across the MIT keeps drawing the attention of a large community in condensed-matter physics [16–26].

Among the many materials featuring a MIT, V_2O_3 is considered a paradigmatic example. Undoped, unstrained bulk V_2O_3 features a MIT at around 160 K, across which the

resistivity changes over six orders of magnitude [27,28]. The MIT is concomitant with a structural phase transition (SPT) between the high-temperature corundum and low-temperature monoclinic structures [Fig. 1(a)] [29]. The corundum metallic phase has a hexagonal unit cell. Across the SPT, the corundum c -lattice parameter shortens (-0.36%), the c -plane area expands ($+1.29\%$), and the c axis tilts slightly, i.e., the angle between the a and c axes becomes less than 90° . This monoclinic tilt can happen along three equivalent directions, and therefore three monoclinic twins are possible.

In thin films, V_2O_3 can be strained and confined laterally by the substrate. This puts constraints on the SPT, which can no longer take place freely. Because of the SPT, the nucleation of insulating–metallic domains within the film results in compressive strain being applied to the neighboring areas, which can either promote or hinder the MIT in those areas [30]. When insulating domains nucleate, they usually arrange in an alternating pattern that minimizes strain [9,22,23]. Domain self-organization due to strain accommodation is not unique to V_2O_3 and is often observed in multiple systems featuring a SPT, such as VO_2 [14,31–33], rare-earth nickelates [34,35], manganites [36], and FeRh [37].

The case of V_2O_3 is especially striking given the big change in lattice constants, which is largest on the base of the hexagonal unit cell [29]. In 001-oriented V_2O_3 films, that base

*These authors contributed equally to this work.

[†]Present address: Department of Interface Science, Fritz-Haber-Institut der Max-Planck-Gesellschaft, Faradayweg 4-6, 14195 Berlin, Germany.

[‡]Corresponding author: zhu@bnl.gov

[§]Corresponding author: javier.delvalle@uniovi.es

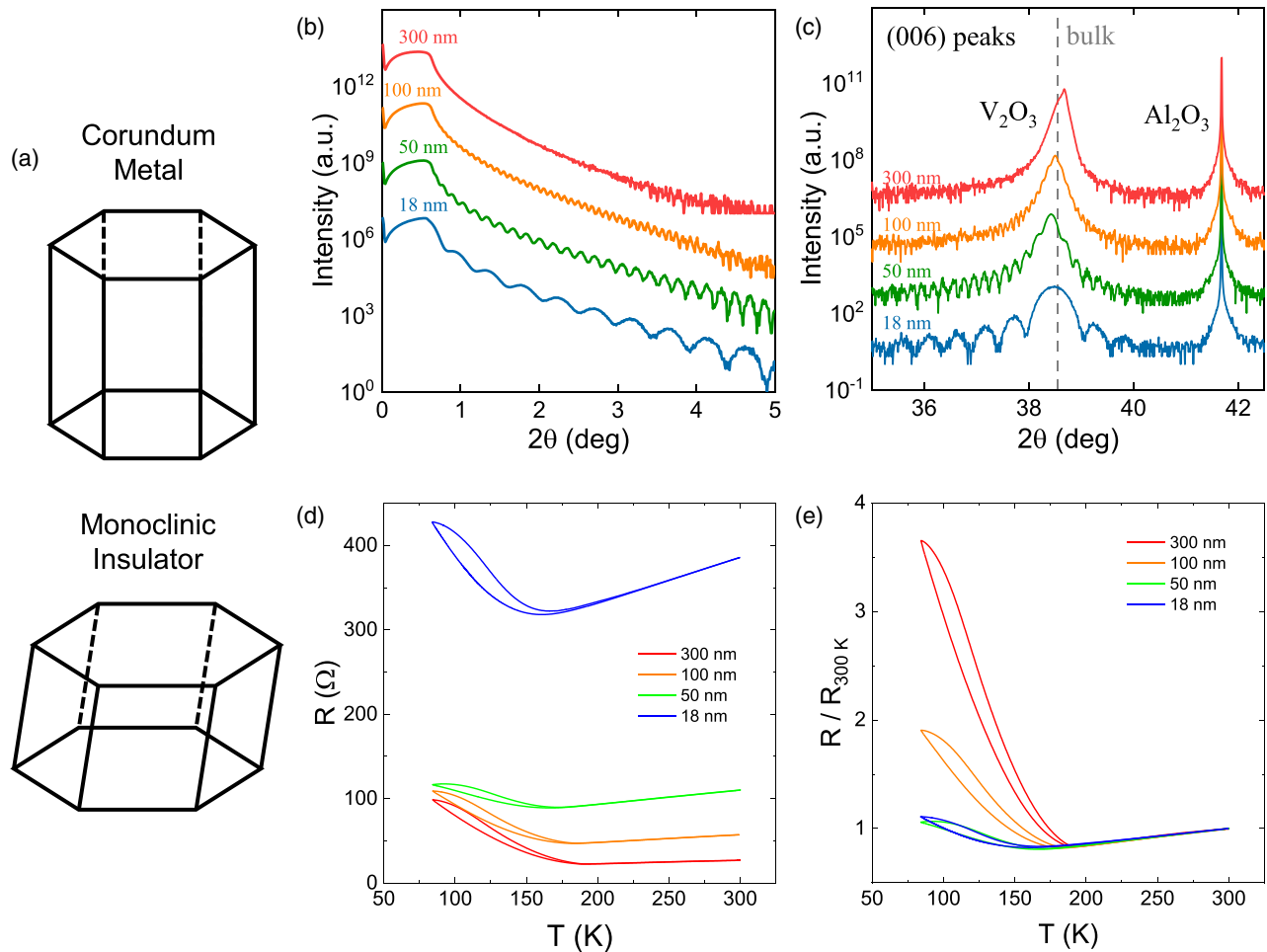


FIG. 1. (a) Schematic representation of the V_2O_3 unit cell in the corundum and monoclinic phases. (b) X-ray reflectivity of four (001)-oriented V_2O_3 films grown on (001)-oriented sapphire, with thicknesses ranging between 18 and 300 nm. Measurements were done at room temperature. (c) θ - 2θ scans around the 006 peaks of the V_2O_3 films and the sapphire substrates. The vertical dashed line shows the position of the (006) peak for relaxed bulk V_2O_3 . Measurements were done at room temperature. (d) Two-point resistance vs temperature for the four V_2O_3 films. (e) Resistance normalized by the film's resistance at 300 K, to better compare the MIT suppression.

is parallel to the plane, and is therefore confined in size by the substrate. As a result, the film cannot expand, and the MIT is strongly suppressed. The observed degree of suppression can range from an incomplete film transformation across the MIT to a full suppression of the insulating state and persisting metallic phase down to 0 K.

The intense self-strain that develops during domain nucleation provides an unconventional platform to study the pressure-temperature phase diagram, with access to both positive- and negative-pressure regimes, and can stabilize novel phases without any external driving force [30,38]. For instance, it was recently shown that the paramagnetic insulator phase in pure V_2O_3 , not stable at room pressure, can be stabilized in thin films by imposing strain on the (100) corundum plane [38]. Furthermore, epitaxy-induced structural locking has been proposed to decouple the MIT from the SPT. Several works have reported such decoupling in related compound VO_2 [16,39] and, more recently, also in (001)-oriented V_2O_3 [40,41].

Direct visualization of how domains nucleate and grow is key for understanding and exploiting the complex phase

diagram of these highly correlated systems. Planar (top-view) imaging of the transition has been thoroughly reported using different probes [23,42]. These techniques, however, only offer a partial description since they are not sensitive to variations along the film thickness. A complete picture requires cross-sectional imaging that shows the phase-transition extent across the thickness of the film.

In this work we provide a complete picture of domain nucleation and growth in strongly self-strained, (001)-oriented V_2O_3 films. We combined two techniques that allowed us to capture planar as well as transversal snapshots of the MIT: photoelectron emission microscopy (PEEM) and scanning electron transmission microscopy (STEM). We observed that insulating domains first nucleate at the surface of the film where strain is lowest and grow downwards and laterally until they stop at around a critical thickness of 50 nm from the substrate-film interface. The existence of a critical thickness prevents thinner films from nucleating any insulating phase within their interior. PEEM imaging, however, revealed a thin superficial layer on the film's surface where the MIT could take place, even for the thinnest films. Domain

formation here shows very different features compared to the bulk of the film.

Our results offer a comprehensive spatially resolved picture of the MIT in strongly strained systems. This information is fundamental for proper interpretation of macroscopic measurements of the MIT properties, and for the strain and epitaxy control and stabilization of electronic and structural phases. On the practical level, engineering the thickness-dependent MIT can simplify the fabrication of out-of-plane switching devices, as the persistent metallic phase region below the critical thickness can be potentially utilized as a native bottom electrode, alleviating the need for conducting substrates or conducting buffer layers.

II. GROWTH, TRANSPORT, AND X-RAY DIFFRACTION

V_2O_3 films were epitaxially grown on top of *c*-cut (001) sapphire (Al_2O_3) substrates using rf magnetron sputtering from a stoichiometric V_2O_3 target. Growth was done in an 8-mTorr Ar atmosphere with a substrate temperature of 700 °C. After growth, the samples were thermally quenched at a rate of around 90 °C/min. Four samples of different thicknesses were grown: 300, 100, 50, and 18 nm. Film thickness was confirmed by x-ray reflectivity measurements [Fig. 1(b)]. Specular x-ray diffraction [XRD, Fig. 1(c)] shows that V_2O_3 films are compressively strained by the underlying substrate, the compression being larger for the thinner films, as expected.

Figure 1(d) shows resistance vs temperature for all four samples, while Fig. 1(e) shows resistance normalized to the 300 K resistance for each sample, so that transport properties can be better compared. In all cases, the usually observed five-to-seven orders of magnitude V_2O_3 MIT is strongly suppressed. The degree of suppression is dependent on the film thickness, as reported before [30]: thinner films show a smaller upturn in resistance, indicating a lower insulating phase fraction in the low-temperature range.

The impact of film thickness on the monoclinic insulator phase formation is further confirmed by low-temperature XRD measurements. Figure 2 and Supplemental Material [43], Fig. S1 show reciprocal-space maps in the vicinity of the (119) and (006) Bragg peaks, respectively. Two samples are shown: 300 and 50 nm. For each case, multiple temperatures between 300 and 93 K are shown. For the thicker film, the single corundum peak loses intensity and partially splits into several peaks as the temperature is lowered. These peaks correspond to the different monoclinic twins of the insulating phase. Therefore, as the temperature goes down, part of the film transitions from corundum to monoclinic. Notice, however, that the central corundum peak does not disappear, retaining around 10% of its initial intensity, which indicates that the structural transition and, consequently, the MIT are incomplete. This explains the moderate resistance upturn in Figs. 1(d) and 1(e) below the $T_C \sim 160$ K.

A very different scenario takes place for the 50-nm sample. The single corundum peak remains at all temperatures, and no sign of monoclinic phase can be detected in the reciprocal-space maps. The corundum peak does, however, lose some intensity at lower temperatures, as can be better seen in the θ - 2θ scans of Supplemental Material [43], Fig. S2. This

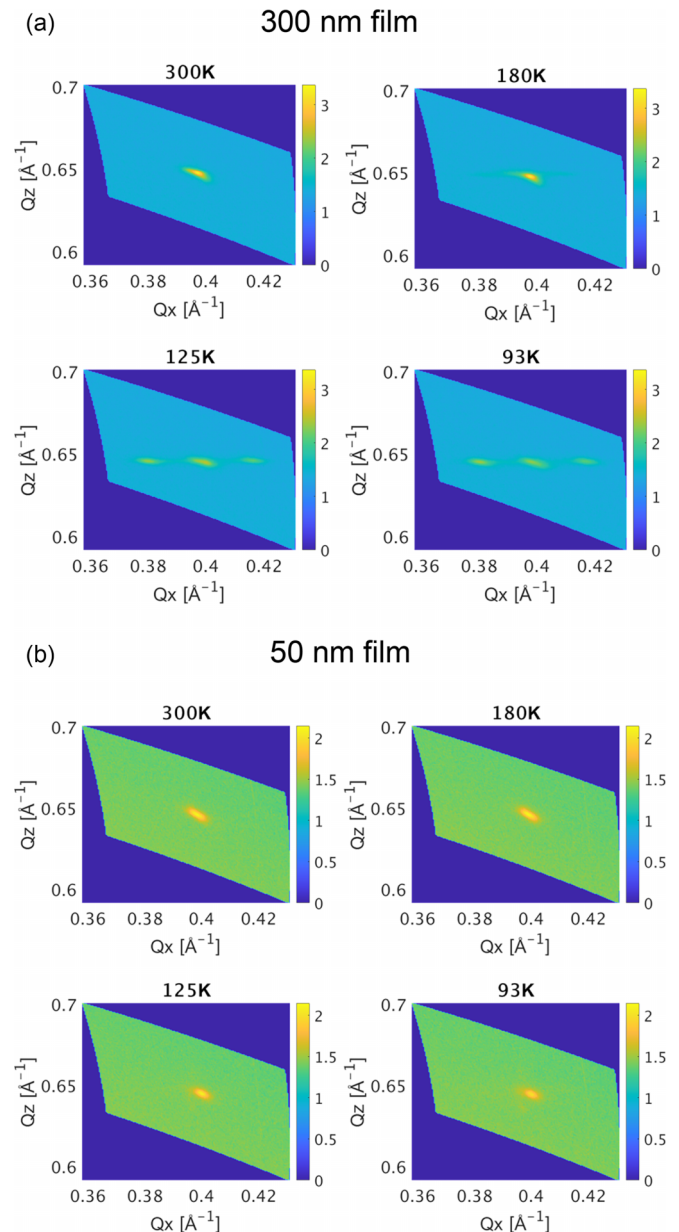


FIG. 2. Reciprocal-space maps around the 119 direction for (a) a 300-nm film and (b) a 50-nm film. Several temperatures are shown. Several twins are possible and visible for the monoclinic phase. No twinning is observed in the corundum phase.

implies that at least some fraction of the corundum phase ($\sim 20\%$) disappears as the temperature is lowered, even though our x-ray-diffraction measurements were not able to detect the formation of the monoclinic phase in the 50-nm films at temperatures down to 93 K.

III. STEM MEASUREMENTS

To understand the spatial distribution of domain nucleation, we performed Cryo-STEM measurements. Thin films were sliced into 120-nm-thick lamellas by means of a focused ion beam and were subsequently imaged using the LN2 Mel-Build sample holder in a double aberration-corrected JEOL

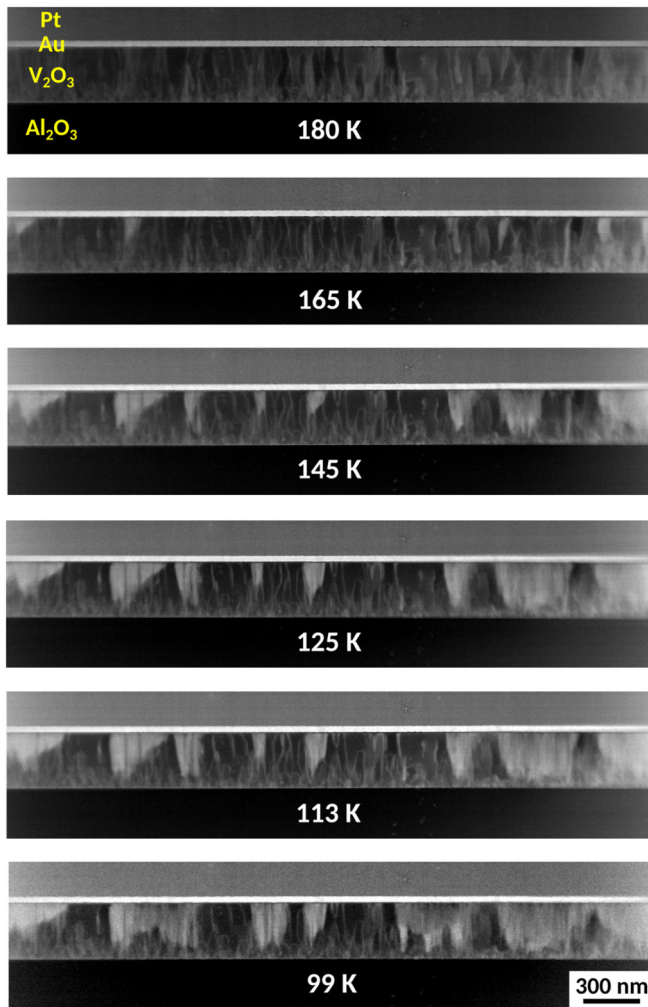


FIG. 3. Cryogenic STEM LAADF electron micrographs of the 300-nm-thick V_2O_3 film from 180 to 99 K. Because LAADF imaging in STEM is very sensitive to lattice distortion (largely diffraction contrast), it is used here to reveal crystalline defects, grain boundaries, and thickness variation as well as to dissociate the corundum and the monoclinic crystal structure of V_2O_3 . The extended bright and dark areas correspond to the monoclinic and the corundum phases of the V_2O_3 material, respectively.

ARM 200F cold FEG microscope, operating at 200 keV in STEM mode (more details in the Supplemental Material [43]).

Figure 3 shows low-angle annular dark-field (LAADF) images of the 300-nm V_2O_3 film from 300 K down to 99 K. This imaging mode is especially sensitive to local lattice distortions such as those surrounding defects and grain boundaries. Columnar vertical film growth is readily observed at all temperatures, giving weak contrast variations. Monoclinic areas give a much stronger contrast due to the large lattice orientation difference, and start being visible at 165 K and below.

Nucleation starts from the top and expands downwards and laterally. The insulating phase does not grow following a flat front; instead, it expands following randomly distributed columnar growth defects. This makes it hard to reproduce the R vs T curves in Fig. 1(d) using a resistor network model. The monoclinic domain expansion slows down as the temperature

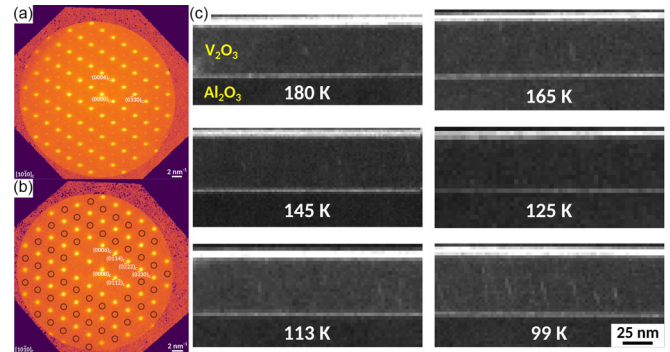


FIG. 4. Four-dimensional STEM characterization of the V_2O_3 films at cryogenic temperature. (a) Locally averaged electron diffraction pattern in log scale recorded at 125 K from a monoclinic V_2O_3 region in the 300-nm-thick film (indexed using the corundum phase notation). (b) Locally averaged electron diffraction pattern in log scale recorded at 125 K from the 50-nm-thick V_2O_3 film. (c) Intensity map from the circled areas in (b) capturing the singularity from the monoclinic phase in the 50-nm V_2O_3 film, from 180 to 99 K.

approaches 100 K. Importantly, monoclinic domains never reach the bottom substrate-film interface and stop their growth around 50 nm from it, which sets the critical thickness of the domain propagation depth inside the film. Supplemental Material [43], Fig. S3 shows similar measurements for the 50-nm V_2O_3 film, i.e., the film right at the critical thickness. No monoclinic phase contrast is visible for any temperature in the STEM imaging, which is in good agreement with XRD measurements in Fig. 2(b).

To further confirm the nucleation of monoclinic domains in the 300-nm-thick V_2O_3 film and to verify the absence of monoclinic regions in the interior of the 50-nm-thick film, we used the four-dimensional (4D)-STEM method [44], which allowed us to obtain local diffraction patterns with 5-nm spatial resolution. Figure 4(a) shows one of such patterns taken in a monoclinic domain of the 300-nm-thick film. Note that in addition to the array of intense peaks, similar to the one observed for the metallic corundum structure, weaker satellite peaks are discernible in between. These are a hallmark of the monoclinic distortions. Figure 4(b) shows a local diffraction pattern of the 50-nm film, at 125 K. Extra monoclinic peaks are completely missing, unambiguously ruling out the presence of the monoclinic phase. By repeating this diffraction acquisition in every spot in the field of view it is possible to construct the phase maps shown in Fig. 4(c), which plot the intensity of the satellite peaks circled in Fig. 4(a). From these maps, we can conclude that no monoclinic phase is observed at any temperature in the interior of the 50-nm-thick V_2O_3 film.

IV. STRAIN ANALYSIS

To understand why the monoclinic domains do not propagate below the 50-nm critical distance from the film-substrate interface, we used the 4D-STEM data to perform strain analysis (more information in the Supplemental Material [43]). The obtained strain maps for the 300-nm film at 293 K are shown in Fig. 5(a). E_{xx} refers to strain along the horizontal

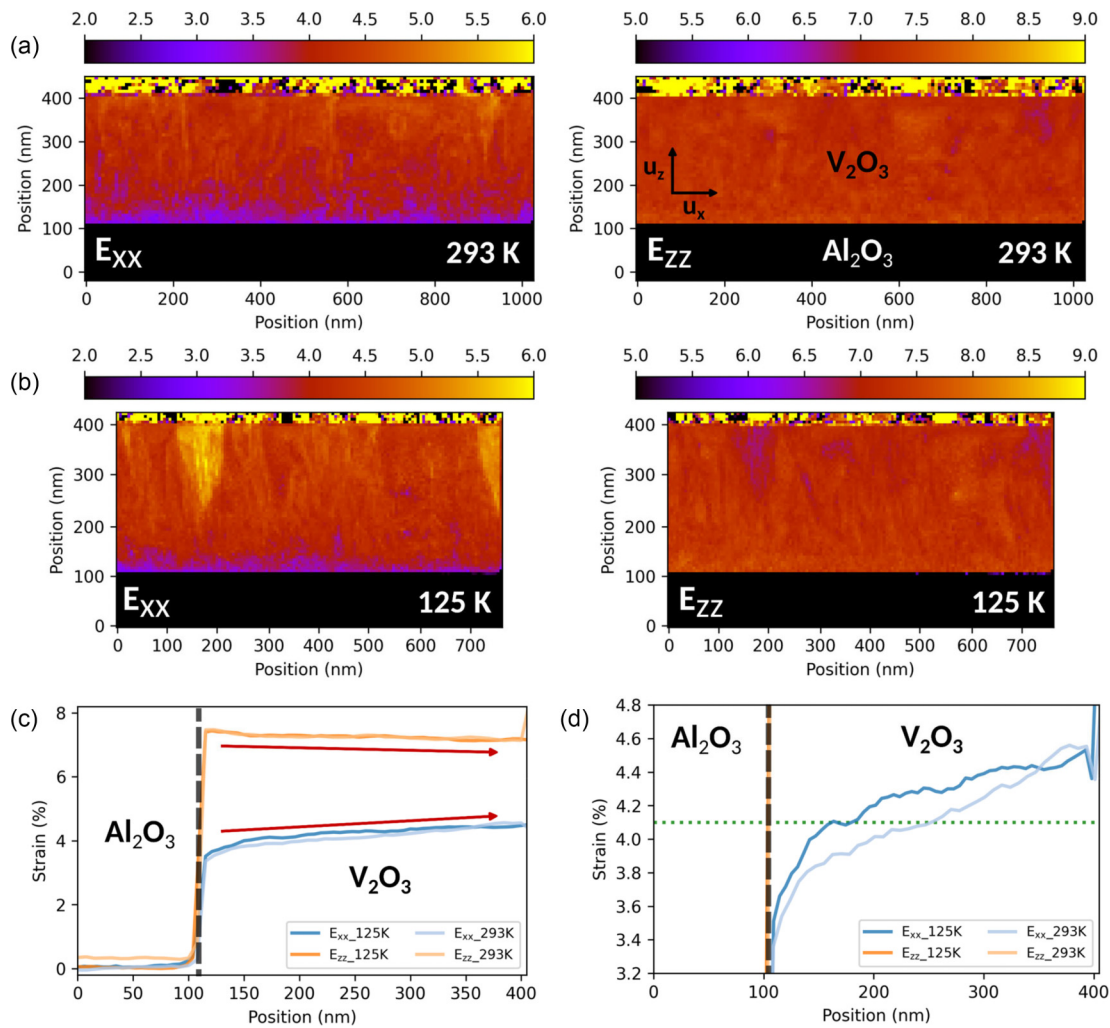


FIG. 5. Strain characterization of the 300-nm-thick V_2O_3 film at (a) 293 K and (b) 125 K. The different panels correspond to uniaxial relative deformation maps (E_{xx} , E_{zz}) of the V_2O_3 film, using the sapphire substrate as the reference. (c) Vertical E_{xx} and E_{zz} profile lines, integrated along the x axis. Both 293 and 125 K are shown. The vertical black dashed line shows where the interface between substrate and film is. (d) Enlarged plot of the E_{xx} components from (c). Compressive strain increases as the interface is approached. The green dotted line in (c) and (d) marks the expected E_{xx} for the unstrained bulk V_2O_3 relative to the sapphire, as mentioned in the main text.

(in-plane) direction, while E_{zz} refers to the vertical (out-of-plane) direction.

It is important to note that strain values are calculated with respect to the lattice parameters of the sapphire substrate, not with respect to relaxed V_2O_3 . Both metallic V_2O_3 and sapphire have corundum structure, but V_2O_3 has a larger lattice parameter: 4.1% (7.8%) larger in plane (out of plane), respectively, according to the literature's bulk crystal structure parameters [45,46]. Strain values in Fig. 5 are calculated with respect to the substrate. This means that a measured E_{xx} below 4.1% implies compressive strain, since the lattice parameter would be below that of bulk V_2O_3 , while E_{xx} above 4.1% indicates tensile strain. Our calculated E_{xx} is around 3.5% near the substrate interface, so at that location V_2O_3 is subject to a strong in-plane compression.

A clear vertical dependence for E_{xx} can be identified: compressive strain is strongest near the film-substrate interface and slowly decreases along the z direction. This implies that V_2O_3 is compressed along the in-plane direction due

to the sapphire substrate clamping, but the film relaxes with increasing thickness, probably due to the proliferation of defects. As expected from the Poisson effect, E_{zz} follows the opposite behavior, being higher near the substrate and decreasing towards the top of the film. These trends are present at different temperatures [Figs. 5(a) and 5(b)] and can be better appreciated in the vertical line profiles of Fig. 5(c). The E_{zz} vertical gradient leaves a clear imprint in the XRD measurements: thicker films show asymmetric 006 peaks.

It is possible to estimate the magnitude of compressive forces near the bottom interface and check whether these forces are strong enough to completely frustrate the MIT. The monoclinic insulating phase in bulk V_2O_3 is suppressed at hydrostatic pressures above 20 kbar [47]. Figure 5(d) shows a detailed vertical profile of E_{xx} in our films. Approaching the film-substrate interface, E_{xx} sharply drops to values below 3.5%, which, compared to the crystal lattice of bulk V_2O_3 , indicates that the film develops a compressive strain of approximately -0.6% . Taking the V_2O_3 Young's modulus to

be 150 GPa [48], we obtain an in-plane stress of ~ 9 kbar. While this stress is below the expected 20 kbar, we must note that the film is not compressed hydrostatically, but uniaxially and along the direction that expands the most across the MIT. Therefore, it is reasonable to expect that the transition into the insulating phase will be suppressed with noticeably lower compressive stresses, such as the ones we estimate. At the film's surface, on the other hand, E_{xx} is tensile, i.e., the film is expanded in the horizontal plane as compared to the bulk V_2O_3 . Oppositely to the compressive strain, tensile strain is expected to promote the MIT, which explains why the monoclinic domains can form near the film's surface (Fig. 3).

E_{xx} on the film's top surface is around 4.4%, implying that, far from being compressed, V_2O_3 at that location is subjected to tensile strain. While this might seem counterintuitive due to the smaller lattice parameter of sapphire, it can be explained by considering the different thermal expansion coefficients of both materials [29,46]. Film growth is done at high temperatures (700 °C), where lattice parameters are significantly larger than at the measurement temperature. The V_2O_3 -sapphire lattice mismatch is even higher at 700 °C than at room temperature, so the film grows very compressively strained. The top part of the film, however, will be less compressed than the interface. As the sample is cooled down after growth both materials contract, but V_2O_3 contracts faster [29,46], therefore relieving some of the compression. This decompression can get to the point that, for thick films, strain on the top surface changes sign due to the expanding film underneath, resulting in tensile forces [38]. Tensile in-plane strain at the top interface also leaves an imprint on E_{zz} due to the Poisson effect. E_{zz} falls below the bulk value of 7.8%, meaning the c -axis lattice parameter is shorter than bulk on the top of the film. This can be also seen in the XRD measurements on Fig. 1(c): the 006 V_2O_3 peak of the 300-nm film is shifted to higher angles than that of bulk V_2O_3 .

To understand the origin of the counterintuitive tensile strain at the V_2O_3 surface, we estimated the strain magnitude due to the thermal expansion coefficient mismatch between the film and substrate. If the top of the 300-nm V_2O_3 film was completely relaxed at the growth temperature (700 °C), the a -lattice parameter of V_2O_3 would have been around 0.502 nm (extrapolating the data in McWhan *et al.* [29]). Let us consider that during cooldown the film contracts coherently, following the substrate contraction. The Al_2O_3 a axis is 0.5% shorter at room temperature than at 700 °C [46], so the V_2O_3 a axis at the top of the film could be expected to be around 0.499 nm after cooling down. Relaxed bulk V_2O_3 at room temperature has a 0.496-nm a axis, meaning that the top of the film would be under a 0.6% tensile strain, despite being grown epitaxially on a substrate with a smaller lattice parameter. Experimentally we observe a 0.3% tensile strain. The discrepancy is likely due to the assumption that film and substrate expand and contract coherently.

For the insulating phase to nucleate, the film needs to accommodate a large in-plane expansion associated with the corundum-to-monoclinic transition. Such strain accommodation is easier at the top interface, where compressive forces are lowest (or even tensile). Figure 5(b) shows E_{xx} and E_{zz} at 125 K obtained at the same location as the map in Fig. 5(a).

Two monoclinic domains can be clearly identified, leaving an imprint on strain. E_{xx} is much higher and E_{zz} much lower within the domain. From these results we can interpret that insulating areas are subjected to a strong compressive stress, which is larger the closer to the substrate, forcing domains to acquire a wedge shape. Stress increases fast below the critical thickness, preventing the insulating domains from ever reaching the bottom substrate-film interface. While here we obtained a critical thickness of 50 nm, its specific value is expected to depend on the substrate choice and its lattice mismatch with the film. Lower mismatches will likely give rise to lower critical thicknesses.

While STEM data show no monoclinic phase in the interior of the 50-nm V_2O_3 film, resistance data in Fig. 1(b) show an upturn in resistivity at low temperatures, and θ - 2θ scans in Supplemental Material, Fig. S2 show a slight intensity decrease of the corundum structural peak. This suggests that there might be a small fraction of the film that can turn insulating. A closer inspection of the corresponding STEM data (Fig. S3) shows an extremely narrow dark-contrast V_2O_3 layer on the film surface, right beneath the gold protective layer. A similar layer is observed for the 300-nm film (Fig. 3). Due to its small thickness (< 3 nm) and proximity to the gold film, we are not able to gather much information about this layer using the 4-D STEM technique.

V. PEEM MEASUREMENTS

X-ray PEEM, being a surface-sensitive technique with limited probing depth (2–3 nm), is an ideal tool to study the properties of the upper surface layer of V_2O_3 . Shining x-rays with photon energies corresponding to the resonant vanadium L -edge induces strong photoemission from the sample surface. The number of electrons ejected is proportional to the x-ray absorption (XAS). Since different V_2O_3 phases feature different XAS spectra, photoelectron intensity maps can reveal the distribution of insulating-metallic domains [42]. To investigate the possible transition in the surface layer of the 50-nm-thick V_2O_3 film, we performed temperature-dependent PEEM measurements at the UE49-PGMa beamline at the BESSY II synchrotron.

Metallic V_2O_3 has two d electrons and three overlapping bands at the Fermi surface: two degenerate e_g bands arising from d orbitals oriented in the plane, and an a_{1g} band coming from a d orbital pointing out of plane [49]. As a result, there is some x-ray linear dichroism (XLD): the XAS spectrum differs slightly depending on the orientation of the electric-field vector of the incoming linearly polarized beam. Figures 6(a) and 6(c) show XAS at 190 K for the 300- and 50-nm films, respectively. XAS were measured using radiation polarized either horizontally (H) or vertically (V), which in our experimental setup corresponds to the electric-field vector being almost orthogonal and almost parallel to the sample's surface, respectively. We say that it is "almost" perpendicular or parallel because the incoming beam has a grazing incidence angle of 16° .

Within the metallic state, $XLD = V/H$ is close to 1. There is little dichroism. When V_2O_3 turns monoclinic at low temperature, the a_{1g} band is pushed up, away from the Fermi surface, losing occupancy. Consequently, the system becomes more

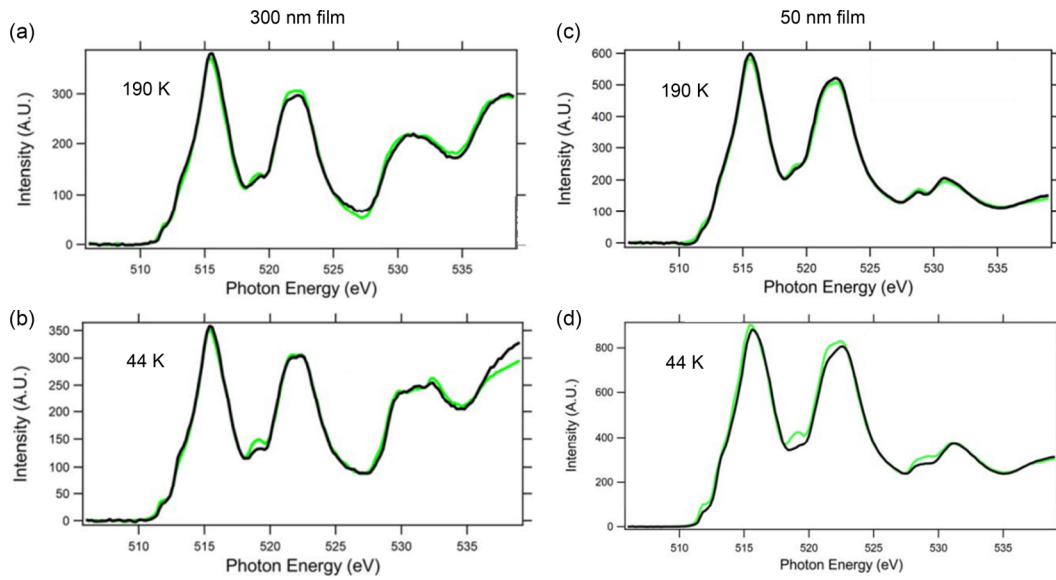


FIG. 6. X-ray absorption near the vanadium L - and oxygen K edges for the (a) 300-nm film at 190 K, (b) 300-nm film at 44 K, (c) 50-nm film at 190 K, and (d) 50-nm film at 44 K. For each panel, scans with light polarized in plane (black) and out of plane (green) are shown.

anisotropic and the XLD is no longer close to 1. This can be seen in Figs. 6(b) and 6(d), which are taken at 44 K. From them, we can see that XLD is largest around 519 eV. Unlike in XRD and STEM measurements, XLD shows large changes as a function of temperature, not only for the 300-nm sample but also for the 50-nm one.

Figure 7(a) shows space-resolved XLD images of the 50-nm-thick film, for different temperatures, for a photon energy of 519.2 eV. While the images are featureless at high temperatures, domains can be clearly distinguished at lower temperatures. Interestingly, these domains appear continuously, becoming increasingly more intense, but showing little changes in size. This is observed both in warmup [Fig. 7(a)] and cooldown (Fig. S4). The zoom into a specific domain shown in Fig. S5 allows to see this effect better.

Three XLD intensity levels can be appreciated, corresponding to three different types of domains. To better understand their nature, we divided the image into three different regions of interest, according to their intensity level. XAS spectra were calculated by integrating over each of these regions. Figures 7(b) and 7(c) show the XAS taken with in-plane (V) and out-of-plane (H) polarized light. The XAS of the three domains is similar for light polarized out of plane, but clearly different for in-plane polarization. Hence, it is reasonable to interpret the presence of these domains as originating from the three possible insulating, monoclinic twins. Twins have the same out-of-plane projection, and therefore similar XAS for out-of-plane polarization. But, their tilts into different in-plane directions have different projections with respect to the incoming in-plane polarized beam, yielding different XAS for in-plane polarization. Interestingly, the film surface is not equally shared by the three domains. Figure S6 shows dichroism histograms of the three regions of interest: “gray” domains, with $V/H \sim 0.95$, make up most of the surface. Further studies are necessary to understand the origin of unequal domain distribution.

VI. DISCUSSION

Our combined PEEM + STEM measurements suggest, on 001-oriented V_2O_3 films, the presence of a thin surface layer where monoclinic domains can form. Superficial domain nucleation seems to happen in a rather different fashion, as compared to bulk nucleation. There are very limited changes in domain size as temperature is decreased far below T_C (Fig. S5) and, contrary to bulk domains, their contrast emerges in a continuous way, a feature more reminiscent of second-order transitions. While we do not fully understand why this layer forms, we anticipate it could be caused by large strain relaxation, or a potential lattice reconstruction near the film’s surface. The presence of this surface layer might explain the resistance upturn at low temperatures, and the small intensity decrease of the corundum structural peaks in the XRD measurements.

These results show that there is a very strong vertical dependence on the nucleation of insulating domains across the MIT. Not taking this into account could lead to incorrect interpretations. For instance, our XRD results show that 50-nm V_2O_3 films do not feature any monoclinic phase (albeit with a small reduction in corundum peak intensity). But, our PEEM measurements, which are sensitive to the electronic structure, suggest the formation of an insulating phase, or at least a phase with different orbital symmetry. Without considering variations along the vertical direction, one might have been erroneously led to identify a decoupling between the MIT and the SPT.

From the practical point of view, our observation of a critical thickness can enable an unconventional way to fabricate out-of-plane MIT switching devices. Presently, most studies of the MIT switching utilize a planar device geometry. Planar geometry works well for exploring individual device performance, but it is not optimal for large-scale integration. Fabrication of out-of-plane devices requires growing the MIT film on a conducting substrate or buffering the insulating

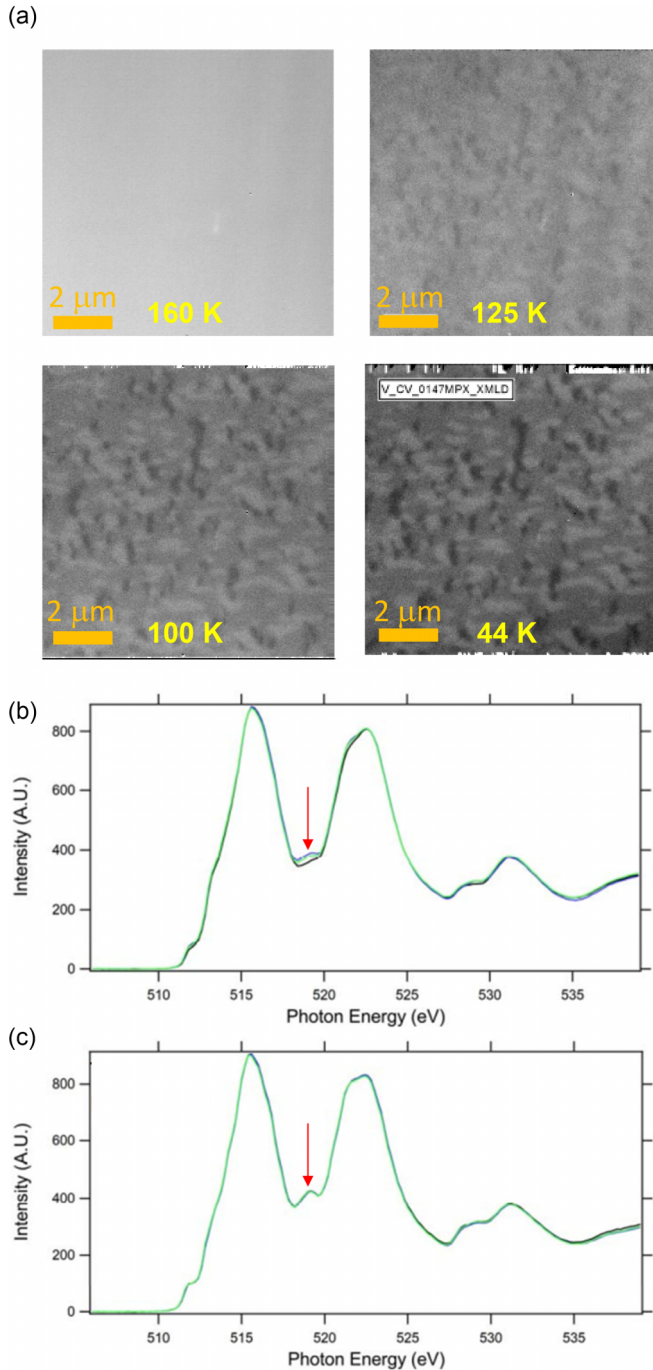


FIG. 7. (a) XLD (V/H) images of the 50-nm film with an incoming beam energy of 519.2 eV. Several temperatures are shown. Temperature scanning was done by increasing temperature. Cooldown measurements are shown in Fig. S4. (b) X-ray absorption for the 50-nm film at 44 K with light polarized in plane. The three scans correspond to three regions of interest (contrast domains) in the PEEM map. These were chosen in accordance with the three domain intensities observed. (c) X-ray absorption for the 50-nm film at 44 K with light polarized out of plane. The three scans correspond to three regions of interest (contrast domains) observed in the PEEM map. These were chosen in accordance with the three intensity domains observed. Red arrows in (b) and (c) indicate the energy where the scans in (a) were measured.

substrate with a conducting layer, which is often detrimental to the MIT film growth as structurally matching conducting substrates or buffer layers are not readily available. Our findings that under appropriate strain conditions, only the top film region undergoes the MIT, while the bottom region always remains metallic, alleviate the need of having a conducting substrate–buffer layer. An out-of-plane switching device can be, in principle, made by fabricating a top metal electrode and utilizing the persistent metallic bottom region as a native electrode. As many MIT materials undergo a coinciding SPT, it can be expected that critical thickness of the transition propagation into the interior of the film can be engineered in other materials beyond V_2O_3 by appropriately choosing the film–substrate epitaxial relation to impose constraints on the SPT and force the bottom region of the film to remain in the metallic state.

VII. CONCLUSIONS

We have performed a thorough characterization of domain nucleation and growth across the phase transition in self-strained, (001)-oriented V_2O_3 films using a combination of STEM and PEEM measurements. We observed that domain nucleation starts where strain is lowest, at the surface of the film. As the temperature is lowered, insulating monoclinic domains grow downwards and laterally, without ever reaching the bottom part of the film likely due to the high compressive stress. For films less than 50 nm thick, insulating domains cannot nucleate in the interior of the film. However, PEEM measurements reveal the existence of a superficial layer at the top electrode in which insulating phase can form, regardless of film thickness. Surprisingly, surface-domain formation shows very different features when compared to that in the interior of the film. Surface domains do not experience large changes in size with varying temperature, and their contrast emerges gradually, resembling a continuous phase transition. These results give fundamental spatially resolved insight into the MIT of strongly self-strained systems. In turn, this is crucial information for stabilizing high-pressure phases in these systems, and for the development of MIT-based devices, key for several technologies.

ACKNOWLEDGMENTS

We thank the Helmholtz-Zentrum Berlin für Materialien und Energie for the allocation of synchrotron radiation beamtime. Sample growth and STEM measurements were funded as part of the Quantum Materials for Energy Efficient Neuro-morphic Computing (Q-MEEN-C) Energy Frontier Research Center (EFRC), supported by the U.S. Department of Energy (DOE), Office of Science, Basic Energy Sciences under Award No. DE-SC0019273. The electron microscopy work done at BNL was also supported by the U.S. DOE, Basic Energy Sciences, Materials Science and Engineering Division under Contract No. DE-SC0012704. Allocation of beamtime from the BESSY II synchrotron with Proposal No. 201–09373-ST is gratefully acknowledged. Lab-based XRD measurements were supported by the European Union’s Horizon Europe research and innovation program under Grant

Agreement No. 101039986– “Highly Energy-Efficient Resistive Switching in Defect- and Strain- Engineered Mott Insulators for Neuromorphic Computing Applications.” J.d.V. was supported by the Spanish Ministry of Science through a Ramón y Cajal Fellowship (Grant No. RYC2021-

030952-I) and by the Asturias FICYT under Grant No. AYUD/2021/51185 with the support of FEDER funds.

Views and opinions expressed herein are those of the authors only and do not necessarily reflect those of the European Union or the European research council.

-
- [1] K. Tang, K. Dong, J. Li, M. P. Gordon, H. Kim F. G. Reichertz, Y. Rho, Q. Wang, C.-Y. Lin, C. P. Grigoropoulos, A. Javey, J. J. Urban, J. Yao, R. Levinson, and J. Wu, Temperature-adaptive radiative coating for all-season household thermal regulation, *Science* **374**, 1504 (2021).
- [2] M. D. Pickett, G. Medeiros-Ribeiro, and R. S. Williams, A scalable neuristor built with Mott memristors, *Nat. Mater.* **12**, 114 (2013).
- [3] W. Yi, K. K. Tsang, S. K. Lam, X. Bai, J. A. Crowell, and E. A. Flores, Biological plausibility and stochasticity in scalable VO₂ active memristor neurons, *Nat. Commun.* **9**, 4661 (2018).
- [4] P. Salev, J. Del Valle, Y. Kalcheim, and I. K. Schuller, Giant nonvolatile resistive switching in a mott oxide and ferroelectric hybrid, *Proc. Natl. Acad. Sci. USA* **116**, 8798 (2019).
- [5] H.-T. Zhang, T. J. Park, A. N. M. N. Islam, D. S. J. Tran, S. Manna, Q. Wang, S. Mondal, H. Yu, S. Banik, S. Cheng, H. Zhou, S. Gamage, S. Mahapatra, Y. Zhu, Y. Abate, N. Jiang, S. K. R. S. Sankaranarayanan, A. Sengupta, C. Teuscher, and S. Ramanathan, Reconfigurable perovskite nickelate electronics for artificial intelligence, *Science* **375**, 533 (2022).
- [6] A. Ronchi, P. Franceschini, P. Homm, M. Gandolfi, G. Ferrini, S. Pagliara, F. Banfi, M. Menghini, J. P. Loquet, and C. Giannetti, Light-assisted resistance collapse in a V₂O₃-based Mott-insulator device, *Phys. Rev. Appl.* **15**, 044023 (2021).
- [7] J. del Valle, N. Vargas, R. Rocco, P. Salev, Y. Kalcheim, P. N. Lapa, C. Adda, M.-H. Lee, P. Y. Wang, L. Fratino, M. J. Rozenberg, and I. K. Schuller, Spatiotemporal characterization of the field-induced insulator-to-metal transition, *Science* **373**, 907 (2021).
- [8] J. S. Brockman, L. Gao, B. Hughes, C. T. Rettner, M. G. Samant, K. P. Roche, and S. S. P. Parkin, Subnanosecond incubation times for electric-field-induced metallization of a correlated electron oxide, *Nat. Nanotechnol.* **9**, 453 (2014).
- [9] M. Lange, S. Guénon, Y. Kalcheim, T. Luibrand, N. M. Vargas, D. Schwebius, R. Kleiner, I. K. Schuller, and D. Koelle, Imaging of electrothermal filament formation in a Mott insulator, *Phys. Rev. Appl.* **16**, 054027 (2021).
- [10] S. Kumar, J. P. Strachan, and R. S. Williams, Chaotic dynamics in nanoscale NbO₂ Mott memristors for analogue computing, *Nature (London)* **548**, 318 (2017).
- [11] J. del Valle, P. Salev, S. Gariglio, Y. Kalcheim, I. K. Schuller, and J.-M. Triscone, Generation of tunable stochastic sequences using the insulator-metal transition, *Nano Lett.* **22**, 1251 (2022).
- [12] S. Cuffe, J. John, Z. Zhang, J. Parra, J. Sun, R. Orobtcouk, S. Ramanathan, and P. Sanchis, VO₂ nanophotonics, *APL Photon.* **5**, 110901 (2020).
- [13] N. Manca, L. Pellegrino, T. Kanki, S. Yamasaki, H. Tanaka, A. S. Siri, and D. Marré, Programmable mechanical resonances in MEMS by localized joule heating of phase change materials, *Adv. Mater.* **25**, 6430 (2013).
- [14] N. Manca, T. Kanki, F. Endo, D. Marré, and L. Pellegrino, Planar nanoactuators based on VO₂ phase transition, *Nano Lett.* **20**, 7251 (2020).
- [15] N. Manca, T. Kanki, F. Endo, E. Ragucci, L. Pellegrino, and D. Marré, Anisotropic temperature-driven strain dynamics in VO₂ solid-state microactuators, *ACS Appl. Electron. Mater.* **3**, 211 (2021).
- [16] D. Lee, B. Chung, Y. Shi, G.-Y. Kim, N. Campbell, F. Xue, K. Song, S.-Y. Choi, J. P. Podkaminer, T. H. Kim, P. J. Ryan, J.-W. Kim, T. R. Paudel, J.-H. Kang, J. W. Spinuzzi, D. A. Tenne, E. Y. Tsymbal, M. S. Rzechowski, L. Q. Chen, J. Lee, and C. B. Eom, Isostructural metal-insulator transition in VO₂, *Science* **362**, 1037 (2018).
- [17] S. Biermann, A. Poteryaev, A. I. Lichtenstein, and A. Georges, Dynamical singlets and correlation-assisted Peierls transition in VO₂, *Phys. Rev. Lett.* **94**, 026404 (2005).
- [18] V. R. Morrison, R. P. Chatelain, K. L. Tiwari, A. Hendaoui, A. Bruhács, M. Chaker, and B. J. Siwick, A photoinduced metal-like phase of monoclinic VO₂ revealed by ultrafast electron diffraction, *Science* **346**, 445 (2014).
- [19] L. Vidas, D. Schick, E. Martínez, D. Perez-Salinas, A. Ramos-Álvarez, S. Cichy, S. Batlle-Porro, A. S. Johnson, K. A. Hallman, R. F. Haglund, Jr., and S. Wall, Does VO₂ host a transient monoclinic metallic phase? *Phys. Rev. X* **10**, 031047 (2020).
- [20] S. Wall, S. Yang, L. Vidas, M. Chollet, J. M. Glowina, M. Kozina, T. Katayama, T. Henighan, M. Jiang, T. A. Miller, D. A. Reis, L. A. Boatner, O. Delaire, and M. Trigo, Ultrafast disordering of vanadium dimers in photoexcited VO₂, *Science* **362**, 572 (2018).
- [21] M. Thees, M.-H. Lee, R. L. Bouwmeester, P. H. Rezende-Gocalves, E. David, A. Zimmers, F. Fortuna, E. Frantzeskakis, N. M. Vargas, Y. Kalcheim, P. Le Fèvre, K. Horiba, H. Kumigashira, S. Biermann, J. Trastoy, M. J. Rozenberg, I. K. Schuller, and A. F. Santander-Syro, Imaging the itinerant-to-localized transmutation of electrons across the metal-to-insulator transition in V₂O₃, *Sci. Adv.* **7**, 1164 (2021).
- [22] S. Lupi, L. Baldassarre, B. Mansart, A. Perucchi, A. Barinov, P. Dudin, E. Papalazarou, F. Rodolakis, J. -P. Rueff, J. -P. Itié, S. Ravy, D. Nicoletti, P. Postorino, P. Hansmann, N. Parragh, A. Toschi, T. Saha-Dasgupta, O. K. Andersen, G. Sangiovanni, K. Held, and M. Marsi, A microscopic view on the Mott transition in chromium-doped V₂O₃, *Nat. Commun.* **1**, 105 (2010).
- [23] A. S. McLeod, E. van Heumen, J. G. Ramirez, S. Wang, T. Saerbeck, S. Guenon, M. Goldflam, L. Anderegg, P. Kelly, A. Mueller, M. K. Liu, Ivan K. Schuller, and D. N. Basov, Nanotextured phase coexistence in the correlated insulator V₂O₃, *Nat. Phys.* **13**, 80 (2017).
- [24] Y. Kalcheim, N. Butakov, N. M. Vargas, M. H. Lee, J. Del Valle, J. Trastoy, P. Salev, J. Schuller, and I. K. Schuller, Robust

- coupling between structural and electronic transitions in a mott material, *Phys. Rev. Lett.* **122**, 057601 (2019).
- [25] Y. Ding, C.-C. Chen, Q. Zeng, H.-S. Kim, M. J. Han, M. Balasubramanian, R. Gordon, F. Li, L. Bai, D. Popov, S. M. Heald, T. Gog, H.-K. Mao, and M. van Veenendaal, Novel high-pressure monoclinic metallic phase of V_2O_3 , *Phys. Rev. Lett.* **112**, 056401 (2014).
- [26] S. Catalano, M. Gibert, J. Fowlie, J. Iñiguez, J. M. Triscone, and J. Kreisel, Rare-earth nickelates $RNiO_3$: Thin films and heterostructures, *Rep. Prog. Phys.* **81**, 046501 (2018).
- [27] M. Imada, A. Fujimori, and Y. Tokura, Metal-insulator transitions, *Rev. Mod. Phys.* **70**, 1039 (1998).
- [28] F. J. Morin, Oxides which show a metal-to-insulator transition at the Néel temperature, *Phys. Rev. Lett.* **3**, 34 (1959).
- [29] D. B. McWhan and J. P. Remeika, Metal-insulator transition in $V_{1-x}Cr_xO_3$, *Phys. Rev. B* **2**, 3734 (1970).
- [30] Y. Kalcheim, C. Adda, P. Salev, M. H. Lee, N. Ghazikhanian, N. M. Vargas, J. del Valle, and I. K. Schuller, Structural manipulation of phase transitions by self-induced strain in geometrically confined thin films, *Adv. Funct. Mater.* **30**, 2005939 (2020).
- [31] M. M. Qazilbash, M. Brehm, B.-G. Chae, P.-C. Ho, G. O. Andreev, B.-J. Kim, S. J. Yun, A. V. Balatsky, M. B. Maple, F. Keilmann, H.-T. Kim, and D. N. Basov, Mott transition in VO_2 revealed by infrared spectroscopy and nano-imaging, *Science* **318**, 1750 (2007).
- [32] A. Tselev, E. Strelcov, I. A. Luk'yanchuk, J. D. Budai, J. Z. Tischler, I. N. Ivanov, K. Jones, R. Proksch, S. V. Kalinin, and A. Kolmakov, Interplay between ferroelastic and metal-insulator phase transitions in strained quasi-two-dimensional VO_2 nanoplatelets, *Nano Lett.* **10**, 2734 (2010).
- [33] J. Cao, Y. Gu, W. Fan, L. Q. Chen, D. F. Ogletree, K. Chen, N. Tamura, M. Kunz, C. Barrett, J. Seidel, and J. Wu, Extended mapping and exploration of the vanadium dioxide stress-temperature phase diagram, *Nano Lett.* **10**, 2667 (2010).
- [34] G. Mattoni, P. Zubko, F. Maccherozzi, A. J. H. van der Torren, D. B. Boltje, M. Hadjimichael, N. Manca, S. Catalano, M. Gibert, Y. Liu, J. Aarts, J.-M. Triscone, S. S. Dhesi, and A. D. Caviglia, Striped nanoscale phase separation at the metal-insulator transition of heteroepitaxial nickelates, *Nat. Commun.* **7**, 13141 (2016).
- [35] J. H. Lee, F. Trier, T. Cornelissen, D. Preziosi, K. Bouzehouane, S. Fusil, S. Valencia, and M. Bibes, Imaging and harnessing percolation at the metal-insulator transition of $NdNiO_3$ nanogaps, *Nano Lett.* **19**, 7801 (2019).
- [36] L. Zhang, C. Israel, A. Biswas, R. L. Greene, and A. De Lozanne, Direct observation of percolation in a manganite thin film, *Science* **298**, 805 (2002).
- [37] C. Baldasseroni, C. Bordel, A. X. Gray, A. M. Kaiser, F. Kronast, J. Herrero-Albillos, C. M. Schneider, C. S. Fadley, and F. Hellman, Temperature-driven nucleation of ferromagnetic domains in $FeRh$ thin films, *Appl. Phys. Lett.* **100**, 262401 (2012).
- [38] E. Barazani, D. Das, C. Huang, A. Rakshit, C. Saguy, P. Salev, J. del Valle, M. C. Toroker, I. K. Schuller, and Y. Kalcheim, Positive and negative pressure regimes in anisotropically strained V_2O_3 films, *Adv. Funct. Mater.* **33**, 2211801 (2023).
- [39] J. Laverock, S. Kittiwatanakul, A. Zakharov, Y. Niu, B. Chen, S. A. Wolf, J. W. Lu, and K. E. Smith, Direct observation of decoupled structural and electronic transitions and an ambient pressure monocliniclike metallic phase of VO_2 , *Phys. Rev. Lett.* **113**, 216402 (2014).
- [40] F. Mazzola, S. Kumar Chaluvadi, V. Polewczyk, D. Mondal, J. Fujii, P. Rajak, M. Islam, R. Ciancio, L. Barba, M. Fabrizio, G. Rossi, P. Orgiani, and I. Vobornik, Disentangling structural and electronic properties in V_2O_3 thin films: A genuine nonsymmetry breaking mott transition, *Nano Lett.* **22**, 5990 (2022).
- [41] A. Ronchi, P. Franceschini, A. De Poli, P. Homm, A. Fitzpatrick, F. Maccherozzi, G. Ferrini, F. Banfi, S. S. Dhesi, M. Menghini, M. Fabrizio, J.-P. Locquet, and G. Giannetti, Nanoscale self-organization and metastable non-thermal metallicity in Mott insulators, *Nat. Commun.* **13**, 3730 (2022).
- [42] A. Ronchi, P. Homm, M. Menghini, P. Franceschini, F. Maccherozzi, F. Banfi, G. Ferrini, F. Cilento, F. Parmigiani, S. S. Dhesi, M. Fabrizio, J.-P. Locquet, and C. Giannetti, Early-stage dynamics of metallic droplets embedded in the nanotextured Mott insulating phase of V_2O_3 , *Phys. Rev. B* **100**, 075111 (2019).
- [43] See Supplemental Material at <http://link.aps.org/supplemental/10.1103/PhysRevMaterials.8.035003> for further x-ray diffraction, stem and peem measurements.
- [44] C. Ophus, Four-dimensional scanning transmission electron microscopy (4D-STEM): From scanning nanodiffraction to ptychography and beyond, *Microsc. Microanal.* **25**, 563 (2019).
- [45] S. V. Ovsyannikov, D. M. Trots, A. V. Kurnosov, W. Morgenroth, H. P. Liermann, and L. Dubrovinsky, Anomalous compression and new high-pressure phases of vanadium sesquioxide, V_2O_3 , *J. Phys.: Condens. Matter* **25**, 385401 (2013).
- [46] H. Chikh, F. S. I. Ahmed, A. Afir, and A. Pialoux, In-situ X-ray diffraction study of alumina $\alpha-Al_2O_3$ thermal behavior under dynamic vacuum and constant flow of nitrogen, *J. Alloys Compd.* **654**, 509 (2016).
- [47] D. B. McWhan, A. Menth, J. P. Remeika, W. F. Brinkman, and T. M. Rice, Metal-insulator transitions in pure and doped V_2O_3 , *Phys. Rev. B* **7**, 1920 (1973).
- [48] N. Alyabyeva, J. Sakai, M. Bavencoffe, J. Wolfman, P. Limelette, H. Funakubo, and A. Ruyter, Metal-insulator transition in V_2O_3 thin film caused by tip-induced strain, *Appl. Phys. Lett.* **113**, 241603 (2018).
- [49] J.-H. Park, L. H. Tjeng, A. Tanaka, J. W. Allen, C. T. Chen, P. Metcalf, J. M. Honig, F. M. F. de Groot, and G. A. Sawatzky, Spin and orbital occupation and phase transitions in V_2O_3 , *Phys. Rev. B* **61**, 11506 (2000).